Spin-Chirality-Driven Multiferroicity in van der Waals Monolayers

Chao Liu,[1,2,3,4] Wei Ren,[1,3,*] and Silvia Picozzi[2]

[1]Institute for Quantum Science and Technology, International Centre of Quantum and Molecular Structures, State Key Laboratory of Advanced Special Steel, Shanghai Key Laboratory of High Temperature Superconductors, Physics Department, Shanghai University, Shanghai 200444, China

[2]Consiglio Nazionale delle Ricerche (CNR-SPIN), Unità di Ricerca presso Terzo di Chieti, c/o Università G. D'Annunzio, I-66100 Chieti, Italy

[3]Zhejiang Laboratory, Hangzhou 311100, China

[4]Hefei National Research Center for Physical Sciences at the Microscale, University of Science and Technology of China, Hefei, Anhui 230026, China

(Received 27 July 2023; accepted 17 January 2024; published 23 February 2024)

Driven by the expected contribution of two-dimensional multiferroic systems with strong magnetoelectric coupling to the development of multifunctional nanodevices, here we propose, by means of first-principles calculations, vanadium-halide monolayers as a new class of spin-chirality-driven van der Waals multiferroics. The frustrated 120-deg magnetic structure in the triangular lattice induces a ferroelectric polarization perpendicular to the spin-spiral plane, whose sign is switched by a spin-chirality change. It follows that, in the presence of an applied electric field perpendicular to the monolayers, one magnetic chirality can be stabilized over the other, thereby allowing the long-sought electrical control of spin textures. Moreover, we demonstrate the remarkable role of spin-lattice coupling on magnetoelectricity, which adds to the expected contribution of spin-orbit interaction determined by an anion. Indeed, such compounds exhibit sizeable spin-driven structural distortions, thereby promoting the investigation of multifunctional spin-electric-lattice couplings.

DOI: 10.1103/PhysRevLett.132.086802

Introduction.—Multiferroics, materials simultaneously showing ferroelectric polarization and magnetic ordering, allow, on one hand, the investigation of fundamentally novel basic-physics phenomena and, on the other hand, their employment in promising functional devices; as such, this class of materials has attracted increasing attention in recent decades [1–3]. In particular, type-II multiferroic systems show ferroelectricity driven by a complex noncentrosymmetric spin configuration and originating from various microscopic mechanisms [4–9]. Notably, upon applying a magnetic field that modulates the magnetic order, the control of ferroelectric polarization can be achieved [10,11]. Type-II multiferroics intrinsically show a strong magnetoelectric coupling, which has been extensively studied. Multiferroicity was initially reported in prototypical $TbMnO_3$ perovskites, benefiting from their spin-spiral configuration; the ferroelectric polarization could be controlled in direction and even reversed in sign through a magnetic field [12]. In addition, the peculiar *E*-type antiferromagnetism (AFM), featuring up-up-down-down spin chains and occurring in the perovskite-type $HoMnO_3$, was also found to induce ferroelectric polarization [13]. Moreover, the triangular lattice AFM configuration, known as "120°" magnetic configuration, was found to be doubly degenerate as for triangular spin chirality [14], and, due to breaking of inversion symmetry, to induce ferroelectric polarization, as proposed for $CuCrO_2$, $RbFe(MoO_4)_2$, and $Ba_3NiNb_2O_9$ [15–18]. However, the vast majority of multiferroic compounds are oxides, therefore limiting the understanding of the role of the chemical identity of the anion in the final multiferroic and magnetoelectric properties.

In parallel, two-dimensional (2D) layered compounds have attracted hectic attention in the field of nanoelectronics, owing to the weak interlayer van der Waals (vdW) interaction, which easily allows the preparation of free-standing monolayers and of complex 2D heterostructures, free from the usual limitations of conventional 3D materials derived from lattice mismatch, atomic interdiffusion at the junctions, etc. The aim of achieving magnetoelectric coupling to 2D layered compounds has been pursued for a long time. The recently reported MnI_2, $CuBr_2$ in the bulk phase and NiI_2 in the few-layers phase, all possess helical magnetic order and show ferroelectric polarization [19–21]. On the other hand, the 120-deg magnetic structures and related magnetoelectric coupling in transition metal halides have not been fully investigated, and the microscopic mechanism driving a possible emergence of ferroelectric polarization remains to be studied.

In this Letter, we predict multiferroicity in 2D VX_2 (X = Cl, Br, I) monolayers with the 120-deg spin structure, whose spin-spiral planes may locate on the (001) and (100) crystalline planes, resulting in a tunable ferroelectric polarization, perpendicular to the spin-spiral plane. Furthermore, the polarization induced by the noncollinear arrangement in

a spin dimer can be expressed via a "magnetoelectric" (or "magnetopolarization") matrix calculated via the four-states method [22]; this procedure clarifies the origin of spin-driven polarization, and leads to comparable results with respect to the modern theory of polarization. In addition, it is found that polarization does not show a simple dependence upon the strength of atomic spin-orbit coupling. We demonstrate that this unexpected feature is partly due to a strong spin-lattice interaction in transition metal halides, which enables even weakly spin-orbit-coupled systems to exhibit a sizeable spin-driven polarization. Additionally, we show that the spin configuration of the bulk counterpart with interlayer antiferromagnetic interaction displays the same spin chirality, and it is thus also capable of exhibiting spin-induced polarization. Finally, considerable ion displacements are also evaluated, with the aim of estimating more realistically the ferroelectric polarization magnitude.

Results and discussion.—VX_2 (X = Cl, Br, I) compounds show the CdI_2-type structure, common to many vdW systems [23], with layers arranged in AA stacking, as seen in Fig. 1(a). Each transition metal cation is octahedrally coordinated with six surrounding nearest anions, and the vanadium cations (V^{2+}), i.e., the source of magnetism ($S = 3/2$), are arranged in a triangular lattice [cf. Fig. 1(a)]. The calculated lattice constants are 3.60, 3.78, and 4.06 Å for the VCl_2, VBr_2, and VI_2 monolayer, respectively, in agreement with corresponding values known for the bulk counterpart [23,24] (cf. Table S1 in Supplemental Material [25]). Here we focus on two possible frustrated magnetic configurations for VX_2 monolayers. In Fig. 1(b), the spin-spiral plane is located within the 2D monolayer, i.e., the (001) plane [denoted below as "(001) AFM"] with magnetic modulation vector $\mathbf{q} = (1/3\,1/3\,0)$, where the angle between the magnetic moment of each V atom and the nearest one is 120 deg, and the directions of all magnetic moments are arranged in plane. As shown in Fig. 1(c), we also consider a spin-spiral plane perpendicular to the 2D monolayer, i.e., the (100) plane (denoted below as "(100) AFM") with magnetic modulation vectors $\mathbf{q} = (1/3\,1/3\,0)$, where each magnetic moment possesses an out-of-plane component. Both configurations exhibit spin chirality that breaks inversion symmetry, allowing for a FE polarization to develop perpendicularly to the spin-spiral plane. It is important to confirm that the three compounds are indeed able to exhibit a 120-deg spin-spiral structure. According to experimental characterizations of the magnetic structure in bulk VX_2, each layer of the three compounds shows a spin-spiral structure, which is parallel to the (100) plane, and there is an AFM coupling between the layers [35–38]. These findings call for an analysis of whether VX_2 halides maintain the spin-spiral order even down to the monolayer limit.

With this aim, various selected magnetic configurations for the three monolayers were calculated, observed in triangular lattices [39], including FM, stripe-type AFM, up-up-down ferrimagnetism, and 120-deg AFM

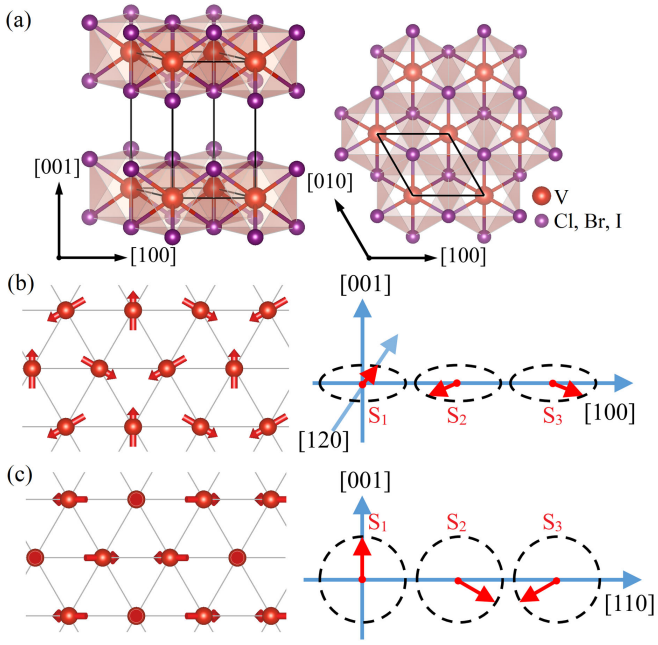

FIG. 1. (a) Structural side view (left panel) and top view (right panel) of transition metal halides. (b),(c) Spin arrangement of 120-deg structure with (b) (001) and (c) (100) spiral planes.

configuration (see related sketch and results shown in Fig. S1 in Supplemental Material [25], where a $\sqrt{3} \times \sqrt{3} \times 1$ supercell was constructed consistent with the periodicity of the spin-spiral structure). Based on the energy comparison obtained by means of simulations based on density functional theory (DFT) complemented with Hubbard-like correlations, we confirmed that the anticipated frustrated configuration is the magnetic ground state for a wide range of U values. The exchange interactions (in the general tensor form) from the first to third nearest neighbor (J_1, J_2 and J_3) of three VX_2 monolayers are calculated using the four-state energy mapping method [22]. The first nearest neighbors all show AFM behavior, the interactions of the second nearest neighbors are almost zero, and sizeable J_3 values (cf. Table S2 [25]) are obtained; this behavior of exchange constants is characteristic of triangular lattices exhibiting a 120-deg frustrated magnetic configuration. Furthermore, we calculated the energy difference between the (001) AFM and (100) AFM, as well as the energy evolution of the bulk and monolayer from (001)-AFM to (100)-AFM configurations (cf. Fig. S2 and Table S3 [25]). The results indicate that (100) AFM is the energetically favorable state for all monolayers and bulks of the three compounds, so that rotating the spin-spiral plane requires crossing a potential barrier. However, the small energy differences simultaneously suggest that the transition between (001) and (100) AFM is achievable with an external magnetic field, thereby in principle realizing the magnetic-field control of the polarization direction, as reported in

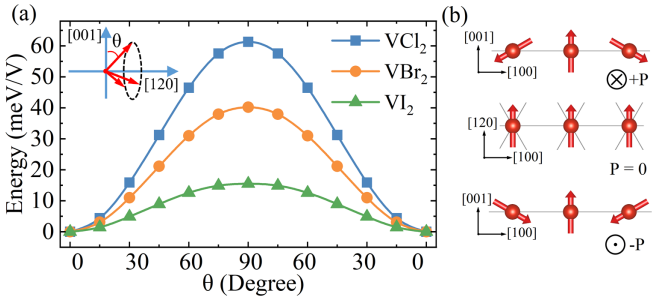

FIG. 2. (a) Potential double well of the three monolayers. The ferromagnetic state is selected to be the paraelectric phase, and the horizontal axis represents the angle between the transition magnetic moments and the initial moments. (b) Magnetic (100)-AFM configuration of the ferroelectric bistable states with clockwise and counterclockwise spiral order exhibiting opposite arrangements of spin chirality. The corresponding polarization is perpendicular to the spin-spiral plane. The intermediate state (ferromagnetic) is also reported in the central panel.

MnI_2, and $CuCrO_2$, where the magnetic field modulates the spin-spiral structure [16,21].

It is worth characterizing the polarization value and the ferroelectric switching mechanism. Both (100)- and (001)-AFM configurations can achieve the polarization switching upon changing the spin chirality. In order to create a switching path, the FM configuration with the magnetic moment along the [001] direction is chosen as the paraelectric phase for (001) AFM, and the FM configuration with [120]-direction magnetic moment is selected for (100) AFM. The total energy evolution of the spin-driven polarization inversion of the (100) AFM of the three compounds is shown in Fig. 2 [those relative to (001) AFM are displayed in Fig. S3 [25]]. The clockwise and counterclockwise rotations of the magnetic moments represent two opposite arrangements of spin chirality. Figure 2 displays the expected potential double well, where the ferroelectric switching is realized by the spin-chirality inversion. Upon confirming nonmetallicity in the entire transition path, we used the modern theory of polarization (i.e., Berry-phase approach) to estimate the polarization values of three monolayers with (001) and (100) AFM reported in Table I. Since there is no unambiguous definition for the "monolayer volume," here we chose the volume of the bulk counterpart of each compound to calculate the final polarization. Polarization values range from 12.2 $\mu C/m^2$ for the VI_2 (001)-AFM to 54.2 $\mu C/m^2$ for VCl_2 (100)-AFM configuration; these values are comparable to those of other magnetoelectric materials, i.e., 17 $\mu C/m^2$ of Cu_2OSeO_3 [40], 31 $\mu C/m^2$ of $CuCl_2$ [41], and 40 $\mu C/m^2$ of $TbMn_2O_5$ [42]. For a more complete description, the band structure and projected density of states of the three monolayers are shown in Fig. S4 [25].

The origin of spin-driven ferroelectric polarization in triangular AFM lattices is nontrivial. The generalized spin current model (gKNB) proposed by Xiang *et al.* is adopted here to study the spin-induced polarization [43] and proved to reliably characterize the magnetoelectric phenomena at play. We recall that, considering the magnetoelectric coupling between the first nearest-neighbor magnetic atoms, the polarization can be expressed as

$$\mathbf{P}^{\mathrm{tot}} = \sum_{\langle i,j \rangle} \mathbf{M}^{ij}(\mathbf{S}_i \times \mathbf{S}_j), \tag{1}$$

where $\mathbf{S}$ represents the normalized spin vector, and $\mathbf{M}$ is a third-order matrix to describe the Cartesian components of polarization produced by a spin dimer in different spin states. This magnetoelectric matrix is determined by performing a four-state mapping analysis by means of DFT simulations. The results for the three halide monolayers are shown in Table II. The matrix elements are represented by the indices of rows and columns, i.e.,

TABLE I. The polarization values of three monolayers with two spin-spiral configurations calculated via the Berry phase (first and second columns) and via the gKNB model (third and fourth columns). Results for different spin-spiral planes are reported in the first and third (second and fourth) columns for the (001)-AFM (100-AFM) spin configuration. The effective volumes (Ω) = 196.31, 228.20, 289.50 $Å^3$ for VCl_2, VBr_2, and VI_2 monolayers, respectively (consistent with the bulk volumes). The monolayer includes three vanadium atoms in order to represent the magnetic configuration.

	Units	DFT (001) AFM	DFT (100) AFM	gKNB (001) AFM	gKNB (100) AFM
VCl_2	$\mu C/m^2$	23.6	60.3	22.3	56.6
	10^{-5} eÅ	28.9	73.9	27.3	69.0
VBr_2	$\mu C/m^2$	22.3	64.8	21.9	63.5
	10^{-5} eÅ	31.7	92.3	31.2	90.4
VI_2	$\mu C/m^2$	12.2	48.1	12.9	52.2
	10^{-5} eÅ	22.0	86.9	23.4	94.3

TABLE II. The magnetoelectric matrix for the three vanadium halides, when considering nearest-neighbors coupling contribution (in units of 10^{-5} eÅ).

	Units (10^{-5} eÅ)		
VCl_2	−1.3	0	0
	0	−16.5	−13.5
	0	4.8	3.5
VBr_2	0.3	0	0
	0	−23.5	−21.0
	0	6.3	4.0
VI_2	4.8	0	0
	0	−29.0	−18.0
	0	5.3	3.0

$$M = \begin{bmatrix} M_{11} & 0 & 0 \\ 0 & M_{22} & M_{23} \\ 0 & M_{32} & M_{33} \end{bmatrix}. \quad (2)$$

The calculated results of total polarization show that, for (001) AFM, $\mathbf{P}^{\mathrm{tot}} = (0\,0\,3\sqrt{3}M_{33})$, and for (100) AFM, $\mathbf{P}^{\mathrm{tot}} = (0\ -3\sqrt{3/2}(M_{11}+M_{22})\,0)$ in Cartesian coordinates. This approach demonstrates that the polarization orientations of the two AFM configurations are consistent with our previous Berry-phase calculations. The polarization of the (001) AFM is dominated by the M_{33} element, while the polarization of the (100) AFM is dominated by the sum of M_{11} and M_{22}. The values for the matrix indicate that VX_2 exhibits considerable deviation from the "standard" (i.e., nongeneralized) spin current model of Katsura, Nagaosa, and Balatsky (KNB) [44], which would predict the only nonzero values to be M_{23} and M_{32}, opposite in value. The polarization magnitudes were further calculated by Eq. (1) and compared with the results obtained from the Berry-phase method, in units of $\mu C/m^2$, as shown in Table I. The results obtained by the two methods are comparable for both (001) and (100) AFM for the three monolayers. Therefore, we infer that, starting from the (crucial) magnetopolarization matrix between neighboring magnetic atoms, reliable polarization values driven by any arbitrary spin configuration can be estimated in such triangular lattices, indicating this approach as an important tool in type-II multiferroics [45,46].

Upon analyzing the polarization results of the (001) and (100) AFM of the three compounds, as well as the magnetopolarization matrices obtained by the gKNB theory, we observe that the trend of polarization of the three compounds is not directly dependent on the strength of the atomic spin-orbit coupling (SOC) determined by the anion. To test the dependence on SOC, we calculated the magnetopolarization matrix when artificially changing the strength of the SOC matrix elements, as shown in Table S4 [25]. All of the matrix elements are identically zero in the case of zero SOC, and increase upon increasing the SOC intensity, elucidating that the polarization of VX_2 is driven by the SOC and affected by its strength. Since the transition metal V atom is considered to show a rather weak SOC and it is the same in the three halides, it is the SOC intensity of the anion that is shown to be important in determining the magnetoelectric coupling. Here we unexpectedly observe that, while the Cl atom exhibits weak atomic SOC, the multiferroicity of VCl_2 is even stronger than that of VI_2. In order to explain this phenomenon, we note that the three compounds have largely different lattice constants, and calculate the magnetopolarization matrices under different lattice constants to explore the possible correlation between structural and multiferroic properties (cf. Table S5 [25]). The estimated electric dipole moments per vanadium (in units of eÅ/V) are shown in Fig. 3, where the dipole moment per V atom is used to

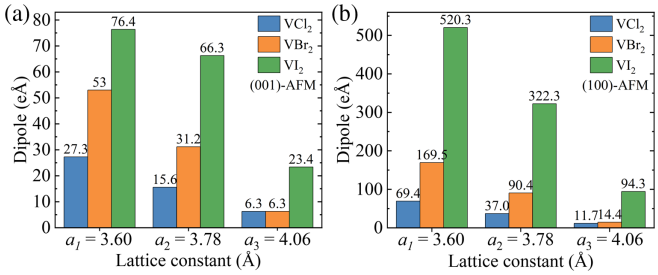

FIG. 3. The lattice-size effect on magnetoelectric coupling, including dipoles induced by (a) (001)- and (b) (100)-AFM configurations. The dipoles of the three compounds are derived from the gKNB theory. Each compound contains three V atoms in the cell.

eliminate the influence of the volume change. We conjecture that the spin-induced electric dipole moment of each compound is affected by the lattice change: Small lattice constants lead to a larger dipole moment, i.e., a larger polarization. Specifically, taking VBr_2 as an example, the lattice parameters of the three compounds are used to calculate the magnetoelectric matrix, the final polarization results for (001) and (100) AFM of three compounds being shown in Fig. 3. The lattice constant of VCl_2 corresponds to a compressive stress of 4.8% for VBr_2, while the lattice constant of VI_2 corresponds to a tensile stress of 7.4% for VBr_2. The results highlight that under a 4.8% compressive stress, the polarization (with respect to the value for the equilibrium lattice constant) from (001) AFM increases by 70% and the polarization from (100) AFM increases by 88%. Furthermore, at a 7.4% tensile stress, the polarization from (001) AFM decreases by 80%, and that of (100) AFM decreases by 84%. These results highlight the crucial effect of the spin-lattice interaction on the magnetoelectricity in VX_2, and explain why VI_2 with a strong SOC effect exhibits a small magnetopolarization. These findings indicate that the SOC effect is indeed the origin of magnetoelectricity, but the spin-lattice effects also play an important role on the magnetoelectric coupling, whose effect exceeds the conventional atomic SOC interaction determined by the anion. Accordingly, there is a potential and feasible way to achieve a strong magnetoelectric system by applying compressive strain, for instance, in strong spin-induced ferroelectric $TbMnO_3$ perovskite [47]. In addition, according to the gKNB theory, we obtained that the third nearest-neighbor magnetoelectric interactions are almost zero for VCl_2 and VBr_2, as shown in Table S6 [25]. For VI_2, showing a heavy ligand with delocalized $5p$ states, the third nearest-neighbor coupling is considered and used to recalculate the polarization for comparison. These results indicate that magnetoelectricity in VX_2 mainly originates from the coupling in the nearest-neighbor spin dimers; however, a longer-ranged coupling effect also deserves consideration in the systems with heavy ligands (iodine). Furthermore, this coupling is

strongly susceptible to the interatomic distance, and it is therefore significantly affected by the lattice.

In addition to what is shown for the monolayers, the multiferroic effects in the bulk counterparts are worthy of attention. As mentioned before, the AA-stacked bulk exhibits interlayer antiferromagnetic coupling. Interestingly, the interlayer spin chirality does not change from plane to plane, which enables the bulk of VX_2 compounds to exhibit polarization. The values calculated by the Berry-phase method, as well as the Hubbard U effect on polarization of bulk and monolayer are shown in Table S7 [25]. The polarization of bulk compounds also follows the dependence on the lattice constant predicted for the monolayer. Notably, the polarizations of bulk and monolayer from (100) AFM are significantly close, whereas the monolayer polarization is much smaller than that of bulk for (001) AFM. The latter behavior might be ascribed to additional electrostatic effects, when the (001)-AFM-induced polarization is parallel to the [001] axis.

Furthermore, the spin-induced atomic displacements are considered in the analysis of spin-driven polarization. This has been previously investigated in magnetoelectric systems dominated by Dzyaloshinskii-Moriya interactions [48–51]; however, not much is known in the triangular lattice 120-deg frustrated structure. As shown in schematic Fig. S5 and Table S8 [25], the polarization value is prominently increased for both the (001) and (100) AFM of VCl_2 and VBr_2 monolayer when including relaxations of the ions in the polar spin-helix configuration [for example, the polarization value of the (100) AFM of VCl_2 increases from 54.2 $\mu C/m^2$ in the centrosymmetric structure to 200.8 $\mu C/m^2$ in the relaxed geometry, i.e., about 3 times in polarization strength]. On the other hand, the final polarizations are reduced for the two magnetic configurations of VI_2 monolayer. These results indicate that the ionic displacements of VX_2 compounds can show a relatively large response to spin-induced ferroelectricity. The inclusion of the ionic displacements likely leads to a more realistic ferroelectric polarization; however, we note that these tiny quantities might be affected by the choice of the exchange-correlation functional.

As expected, an opposite ionic displacement occurs in the corresponding opposite spin-chirality structure. Furthermore, we characterized the magnitude of ionic displacements: The (001) AFM of VCl_2 manifests the largest average ion displacement (i.e., about 3.51×10^{-4} Å, comparable to that of $TbMnO_3$ with strong magnetically induced ionic displacements of about 2.4×10^{-4} Å) [52]. Interestingly, with the same spin chirality, the three compounds have the same sign of final polarization.

Finally, we analyze the polarization switching by an external electric field, since the electric fields effect on magnetoelectric materials is rarely mentioned, despite its utter importance. By applying an electric field to the (001)-AFM-induced polarization parallel to the [001] vacuum layer direction, it is observed that the energy difference between two spin-chirality configurations increases with the electric field strength, as shown in Fig. S6 [25]. As expected, upon applying an electric field, the energy degeneracy between the opposite spin chiralities is removed, and one of the two spin chiralities becomes energetically favorable, thereby accomplishing the long-sought electrical control of spin textures.

Conclusion.—In summary, we have fully characterized the spin-chirality-driven ferroelectric polarization of vanadium-halide monolayers using first-principles calculations, indicating their strong magnetoelectric coupling and magnetostructural distortions as three type-II multiferroics. A change in the spin chirality induces polarization switching, thereby enabling the spin-texture control by an applied electric field. The polarization direction is found to be perpendicular to the spin-spiral plane. Furthermore, by means of the generalized spin current theory, we highlight that the polarization mainly originates from the first nearest-neighbor magnetoelectric interaction, and the calculated gKNB polarization intensity is comparable to that of the Berry-phase approach. The magnetoelectric interaction in VX_2 is strikingly affected by lattice constants and atomic distances, thereby in principle enabling weak SOC systems to exhibit stronger magnetoelectric coupling. In addition, although the three compounds show interlayer AFM coupling, the layers possess the same arrangement of spin chirality and therefore result in a net observable spin-induced polarization in their bulk counterparts. Finally, significant spin-driven ionic displacements are predicted. We hope that the diverse and complex magnetoelectric coupling illustrated in VX_2 compounds will facilitate the advancement of next-generation magnetoelectric devices.

This work was supported by National Natural Science Foundation of China (Grants No. 12074241, No. 12311530675, and No. 52130204), Science and Technology Commission of Shanghai Municipality (Grants No. 22XD1400900, No. 20501130600, and No. 21JC1402700), High Performance Computing Center, Shanghai University, and Key Research Project of Zhejiang Laboratory (Grant No. 2021 PE0AC02). S. P. acknowledges financial support from the Italian Ministry for Research and Education through the PRIN- 2018 project "TWEET: Towards Ferroelectricity in two dimensions" (IT-MIUR Grant No. 2017YCTB59) and via the Next-Generation EU program through the PRIN-2022 "SORBET—Spin-orbit effects in two-dimensional magnets" (IT-MIUR Grant No. 2022ZY8HJY). C. L. acknowledges the support of the China Scholarship Council.

*renwei@shu.edu.cn

[1] W. Eerenstein, N. D. Mathur, and J. F. Scott, Nature (London) **442**, 759 (2006).
[2] N. A. Spaldin and R. Ramesh, Nat. Mater. **18**, 203 (2019).
[3] R. Ramesh and N. A. Spaldin, Nat. Mater. **6**, 21 (2007).

[4] J. P. Hu, Phys. Rev. Lett. **100**, 077202 (2008).
[5] K. Yamauchi and S. Picozzi, Phys. Rev. B **85**, 085131 (2012).
[6] J. H. Yang, Z. L. Li, X. Z. Lu, M. H. Whangbo, S. H. Wei, X. G. Gong, and H. J. Xiang, Phys. Rev. Lett. **109**, 107203 (2012).
[7] S. W. Cheong and M. Mostovoy, Nat. Mater. **6**, 13 (2007).
[8] Y. Tokura, S. Seki, and N. Nagaosa, Rep. Prog. Phys. **77**, 076501 (2014).
[9] S. Dong, H. Xiang, and E. Dagotto, Natl. Sci. Rev. **6**, 629 (2019).
[10] C. W. Nan, G. Liu, Y. H. Lin, and H. D. Chen, Phys. Rev. Lett. **94**, 197203 (2005).
[11] Y. Yamasaki, S. Miyasaka, Y. Kaneko, J. P. He, T. Arima, and Y. Tokura, Phys. Rev. Lett. **96**, 207204 (2006).
[12] T. Kimura, T. Goto, H. Shintani, K. Ishizaka, T. Arima, and Y. Tokura, Nature (London) **426**, 55 (2003).
[13] S. Picozzi, K. Yamauchi, B. Sanyal, I. A. Sergienko, and E. Dagotto, Phys. Rev. Lett. **99**, 227201 (2007).
[14] S. Miyashita and H. Shiba, J. Phys. Soc. Jpn. **53**, 1145 (1984).
[15] H. Mitamura, R. Watanuki, K. Kaneko, N. Onozaki, Y. Amou, S. Kittaka, R. Kobayashi, Y. Shimura, I. Yamamoto, K. Suzuki, S. Chi, and T. Sakakibara, Phys. Rev. Lett. **113**, 147202 (2014).
[16] S. Seki, Y. Onose, and Y. Tokura, Phys. Rev. Lett. **101**, 067204 (2008).
[17] Y. Tokura and S. Seki, Adv. Mater. **22**, 1554 (2010).
[18] J. Hwang, E. S. Choi, F. Ye, C. R. Dela Cruz, Y. Xin, H. D. Zhou, and P. Schlottmann, Phys. Rev. Lett. **109**, 257205 (2012).
[19] Q. Song, C. A. Occhialini, E. Ergeçen, B. Ilyas, D. Amoroso, P. Barone, J. Kapeghian, K. Watanabe, T. Taniguchi, A. S. Botana, S. Picozzi, N. Gedik, and R. Comin, Nature (London) **602**, 601 (2022).
[20] L. Zhao, T. L. Hung, C. C. Li, Y. Y. Chen, M. K. Wu, R. K. Kremer, M. G. Banks, A. Simon, M. H. Whangbo, C. Lee, J. S. Kim, I. Kim, and K. H. Kim, Adv. Mater. **24**, 2469 (2012).
[21] T. Kurumaji, S. Seki, S. Ishiwata, H. Murakawa, Y. Tokunaga, Y. Kaneko, and Y. Tokura, Phys. Rev. Lett. **106**, 167206 (2011).
[22] H. J. Xiang, C. Lee, H. J. Koo, X. G. Gong, and M. H. Whangbo, Dalton Trans. **42**, 823 (2013).
[23] M. A. McGuire, Crystals **7**, 121 (2017).
[24] K. Hirakawa, H. Kadowaki, and K. Ubukoshi, J. Phys. Soc. Jpn. **52**, 1814 (1983).
[25] See Supplemental Material http://link.aps.org/supplemental/10.1103/PhysRevLett.132.086802 for calculation methods, magnetic ground states, magnetic interaction J, energy evolution of the spin-spiral plane rotation, ferroelectric switching potential, electronic structures, effect of changing SOC intensity on polarization, magnetopolarization matrices, polarization value including ions displacement, and effect of an external electric field on polarization, which includes Refs. [26–34].
[26] G. Kresse and J. Furthmüller, Comput. Mater. Sci. **6**, 15 (1996).
[27] S. Grimme, J. Comput. Chem. **27**, 1787 (2006).
[28] P. E. Blochl, Phys. Rev. B **50**, 17953 (1994).
[29] E. Bousquet and N. Spaldin, Phys. Rev. B **82**, 220402(R) (2010).
[30] G. Kresse and J. Furthmüller, Phys. Rev. B **54**, 11169 (1996).
[31] G. Kresse and D. Joubert, Phys. Rev. B **59**, 1758 (1999).
[32] A. I. Liechtenstein, V. I. Anisimov, and J. Zaanen, Phys. Rev. B **52**, R5467 (1995).
[33] L. Wang, T. Maxisch, and G. Ceder, Phys. Rev. B **73**, 195107 (2006).
[34] J. P. Perdew, K. Burke, and M. Ernzerhof, Phys. Rev. Lett. **77**, 3865 (1996).
[35] S. R. Kuindersma, C. Haas, J. P. Sanchez, and R. Al, Solid State Commun. **30**, 403 (1979).
[36] H. Kadowaki, K. Ubukoshi, and K. Hirakawa, J. Phys. Soc. Jpn. **54**, 363 (1985).
[37] H. Kadowaki, K. Ubukoshi, K. Hirakawa, J. L. Martinez, and G. Shirane, J. Phys. Soc. Jpn. **56**, 4027 (1987).
[38] K. Hirakawa, H. Ikeda, H. Kadowaki, and K. Ubukoshi, J. Phys. Soc. Jpn. **52**, 2882 (1983).
[39] J. J. Zhang, L. F. Lin, Y. Zhang, M. H. Wu, B. I. Yakobson, and S. Dong, J. Am. Chem. Soc. **140**, 9768 (2018).
[40] S. Seki, X. Z. Yu, S. Ishiwata, and Y. Tokura, Science **336**, 198 (2012).
[41] S. Seki, T. Kurumaji, S. Ishiwata, H. Matsui, H. Murakawa, Y. Tokunaga, Y. Kaneko, T. Hasegawa, and Y. Tokura, Phys. Rev. B **82**, 064424 (2010).
[42] N. Hur, S. Park, P. A. Sharma, J. S. Ahn, S. Guha, and S. W. Cheong, Nature (London) **429**, 392 (2004).
[43] H. J. Xiang, E. J. Kan, Y. Zhang, M. H. Whangbo, and X. G. Gong, Phys. Rev. Lett. **107**, 157202 (2011).
[44] H. Katsura, N. Nagaosa, and A. V. Balatsky, Phys. Rev. Lett. **95**, 057205 (2005).
[45] H. J. Xiang, P. S. Wang, M. H. Whangbo, and X. G. Gong, Phys. Rev. B **88**, 054404 (2013).
[46] Z. L. Li, M. H. Whangbo, X. G. Gong, and H. J. Xiang, Phys. Rev. B **86**, 174401 (2012).
[47] T. Aoyama, K. Yamauchi, A. Iyama, S. Picozzi, K. Shimizu, and T. Kimura, Nat. Commun. **5**, 4927 (2014).
[48] I. A. Sergienko and E. Dagotto, Phys. Rev. B **73**, 094434 (2006).
[49] A. B. Harris, J. Appl. Phys. **99**, 08E303 (2006).
[50] C. D. Hu, Phys. Rev. B **77**, 174418 (2008).
[51] A. Malashevich and D. Vanderbilt, Phys. Rev. Lett. **101**, 037210 (2008).
[52] H. J. Xiang, S. H. Wei, M. H. Whangbo, and J. L. F. Da Silva, Phys. Rev. Lett. **101**, 037209 (2008).